Chemical Engineering Journal 514 (2025) 162981

Contents lists available at ScienceDirect

Chemical Engineering Journal

journal homepage: www.elsevier.com/locate/cej

Enhancing commercial SOFCs fed directly with ethanol through a modified manganite coating☆

F. Matos de Oliveira [a,b], S. Vecino-Mantilla [b], Z. Hafsi [b], M.V. Barp [b], F. D'Acapito [c], A. Puri [c,d], J. Perez [a], E. Ticianelli [a], M. Lo Faro [b,*]

[a] Instituto de Quimica de São Carlos - USP, Av. Trab. São-carlense, 400, Brazil
[b] Institute of Advanced Energy Technologies (ITAE) of the Italian National Research Council (CNR), Via Salita S. Lucia sopra Contesse 5, 98126 Messina, Italy
[c] CNR-IOM Grenoble c/o ESRF 71 Avenue des Martyrs CS 40220 F-38043 Grenoble Cédex 9, France
[d] Department of Physics and Astronomy, Alma Mater Studiorum – University of Bologna 40127 Bologna, Italy

ARTICLE INFO

Keywords:
Bioethanol
Ruddlesden-Popper
Green deal
REPowerEU
Gas-to-Power

ABSTRACT

In this paper, we propose a novel approach to solve the problem of the fast decay of commercial Solid Oxide Fuel Cells (SOFCs) when directly fueled with dry ethanol. A Nickel Manganite of Lanthanum and Strontium (LSMN−$La_{1.5}Sr_{1.5}Mn_{1.5}Ni_{0.5}O_{7\pm\delta}$) material is used as a coating layer applied to the conventional Ni anode, aimed at modifying the ethanol fuel and suppressing both its craking and carbon deposition that usually occurs on Ni anodes. A thorough electrochemical analysis of the cell at 700 °C, including a durability test, polarization curves (I-V), and Electrochemical Impedance Spectroscopy (EIS) measurements, revealed that the LSMN-modified anode exhibits high stability. As shown by the decreased diffusion constraint observed in the I-V curves after prolonged operation, as well as the presence of three semicircles in the EIS spectrum. This behavior is explained by the occurrence of the so-called *shuttle mechanism*, which is expected to simplify deeply the fuel access into the Ni anode. Structural analysis of the LSMN coating using X-ray Absorption Spectroscopy demonstrated that the perovskite structure of the as-prepared specimen is modified due to Ni exsolution and the partial Mn reduction occurring under operating conditions. Despite the modification taking place on the original perovskite structure, suggesting new Mixed Ionic-Electronic Conduction (MIEC) properties for the LSMN, the experimental evidence presented in this paper proved the effectiveness of the approach of coating commercial SOFCs anode with specific active materials to improve performance.

1. Introduction

Increasing populations and technological advancements result in ever-growing energy consumption [1]. Global electricity demand is expected to increase even faster in 2026, with an average annual growth of 3.4 % in both advanced and emerging countries [2]. Aside from conventional energy demand, there will be another significant increase due to the rapid growth of data centers, artificial intelligence (AI), and cryptocurrency, sectors that are decentralized and growing faster in developing countries with clean and low cost electrical energy [2,3]. Most of the time, and especially in developed countries, the consumption of non-renewable energy results in devastating environmental and economic consequences, such as pollution and climate change, which raises the price of resources globally. Therefore, it is crucial to consider renewable energy alternatives that mitigate the negative impact on the environment and to consider accessible and safe energy technologies. As a result of a combination of government policies and industrial investments, advanced countries should take a leading role in the development of clean energy technologies [3,4].

In this context, energy devices such as SOFCs (Solid Oxide Fuel Cells) hold great promise due to their low cost, ability to convert chemical energy directly into electricity, the absence of noise, superior efficiency compared to conventional technologies, and the modularity that enables them to meet almost any power load requirement [5,6]. In fact, as opposed to combustion-based technologies, which generate mainly thermal and light energy, not electricity at least directly, SOFCs are capable of conveying electrons between redox species in a controlled manner and can achieve up to 80 % efficiency with low pollutant

☆ This article is part of a special issue entitled: 'HYCELTEC2024' published in Chemical Engineering Journal.

* Corresponding author.
E-mail address: lofaro@itae.cnr.it (M. Lo Faro).

https://doi.org/10.1016/j.cej.2025.162981

Available online 27 April 2025

emissions, including almost no NO_x and minimal CO_2, when organic fuels are utilized, including those that are renewable [7,8]. During SOFC operation, the fuel releases its electrons at the anode, creating cationic species that react with oxide ions coming from the cathode to the anode through the electrolyte, while the loop is closed by electrons that circulate externally from the anode to the cathode thus providing useful electricity [9].

Bioenergy is emerging as a viable alternative to fossil fuels and a promising means to reduce CO_2 emissions [10]. Among this type of renewable energy is bioethanol, which can be produced through biomass fermentation [11,12]. When used in advanced technologies like SOFCs, it can contribute to both the economy and the environment since it is a sustainable fuel that is already produced in large quantities for power generation [13–18]. It is currently used as a pure or additive for gasoline in vehicles, but if redirected to high efficiency technologies such as SOFCs, such a biofuel can achieve sustainability while mitigating environmental impact [4,13,19–23]. Additionally, the consolidated capability of transporting this fuel and substantial unrequired contamination with mercaptane, a hazardous component of fuel gas, make this an ideal fuel also for stationary applications based on fuel cells [24,25]. Despite the fact that SOFCs with their high operating temperatures could, in principle, simplify the use of organic fuels, there are still some safety concerns associated with the use of organic fuels in commercial cells This essentially limits large prototypes to running only on hydrogen, or with a pre-reformer and desulfurizer, which increases the complexity of the system as well as the cost of CAPEX and OPEX [26,27].

Currently, commercial SOFCs are manufactured with cells supported on a ceramic–metal composite (cermet) made of Ni and Yttria stabilized Zirconia (YSZ). Because of its excellent conductivity, its thermal expansion coefficient that is compatible with other components needed for the manufacture of a complete SOFC, and its significant electrocatalytic activity, this cermet is well suited to making robust SOFCs [28–30]. In addition, it has excellent stability at high temperatures and low P_{O2}, although it has low redox properties at high P_{O2}, which is its main limitation, for example, for solid oxide electrolysis cells (SOECs) based devices [31–33]. The Ni in such anodes acts as an electrocatalyst, facilitating electron extraction from the fuel (oxidation) and ensuring a continuous path for electrons toward the outside of the cell. However, in order to reach optimal conductivity, a substantial amount of Ni is needed, which generally represents approximately 60 % of the cell's weight [34]. It is instead YSZ oxide that provides the ionic conductivity and thermal stability of this anode. The oxygen percolation is also a key factor in an optimal anode, and to guarantee continuity in its path, the inner part of the anode is more heavily laden with this material, thus generating a higher concentration of triple phase boundaries (TPBs) [35]. Additionally, the YSZ oxide has an optimal thermal expansion coefficient similar to those of the rest of the materials that are used in conventional cells, promoting rigidity in the cermet structure and contributing to reducing the risks of Ni sintering during SOFC operation [36]. As a downside, the high content of Ni used to fabricate SOFCs leads to carbon deposition when using dry organic fuels, thereby lowering the performance of the cells [37–40].

Because of this, ethanol-fed SOFCs still face challenges due to high risks associated with carbon deposits resulting from coking of ethanol over Ni-based anodes [41]. This effect has also been observed in one of our previous papers where a similar bare cell fed ethanol showed rapid decay which renders electrochemical diagnosis [42] impossible and demonstrates what has been reported experimentally and thermodynamically in the literature [15,16,18,43].

Consequently, most of the research efforts in this area are aimed at reducing the operating temperatures in the range 500–700 °C where the thermodynamics are more favorable, and developing new materials to replace or improve the performance of Ni/YSZ cermet [15,44,45]. Obviously, reducing the temperature extends the cell's useful life and decreases the costs of materials used in SOFCs so they can be made cheaper. In spite of this, reducing the operating temperature involves challenges such as decreased oxygen reduction reaction (ORR) kinetics, a high activation energy, and considerable resistance to interfacial polarization [46]. As far as replacing the Ni/YSZ cermet goes, a number of alternatives have already been proposed, including other cermets [47–50] and ceramic anodes [51–54]. However, many of these materials do not exhibit the same level of electronic conductivity or catalytic activity, and many do not have optimal Thermal Expansion Coefficients (TECs), chemical and physical stability at high temperatures. As a result, fabricating cells based on advanced materials is not trivial, which is why commercial SOFCs continue to use the same anode design developed in the 1980 s [55].

One emerging method to improve the performance of a SOFC operating with organic fuel involves adding a catalytic layer to the Ni-anode [56]. In this approach, neither the architecture of SOFCs nor the production chain around this technology are changed. As a result, this approach is similar to attaching a chemical processor directly to a commercial cell anode, providing a synergetic advantage between the two layers [57]. In essence, the coating layer reduces carbon formation risks. This is as a result of an efficient simplification of the initial fuel by initiating a series of reactions which include dehydrogenation and chemical reactions with molecules produced by the supporting Ni-anode, where the syngas is converted into electricity, water, and carbon dioxide. We have described such a mechanism as the *shuttle mechanism* in one of our past papers [42].

Perovskite oxides have proved to be an attractive coating layer for this application due to their strong contrast to fuel cracking mechanisms [58–61]. These materials have acceptable ionic and electronic percolation characteristics derived from their mixed ionic-electronic conductivity (MIEC), in addition to their flexibility in composition, which can be substantially tweaked quite easily. Additionally, their electrical charges and oxygen storage characteristics make them ideal for electrochemical processes and electrocatalysis. As a derived class of such materials, Ruddlesden-Popper (RP) materials have already shown unique properties resulting from the exsolution of cations from their original structure and the sublimation of them as encapsulated spheres on the surface of the materials, which give high chemical reactivity and physical stability [41,62–65]. Unlike the perovskites it derives from, the RP perovskites are composed of rock salt layers (AX) alternating with perovskites-like layers (ABX_3) and have the typical formula of $A_{n+1}B_nX_{3n+1}$. In this structure, alkaline, alkaline-earth or rare-earth metals typically occupy the A site, whereas transition metals are located at B site [62]. Their stratified layer structure, tunable chemical compositions, transport properties, and thermal and mechanical stability make RP perovskites an important emerging class of electrocatalysts [64,66].

In previous works, a LSMN exsolute RP perovskite ($La_{1.5}Sr_{1.5}Mn_{1.5}Ni_{0.5}O_{7\pm\delta}$) was used as the pre-catalytic layer on a conventional Ni/YSZ anode [41,67]. This catalyst had been examined in depth with regard to a biogas-fueled SOFC with the same architecture as that used here. These studies also examined the physico-chemical properties of this material prior to and after prolonged SOFC operation, as well as electrochemical analysis in operation and in the presence of dry biogas. Overall, these studies showed that biogas causes structural and morphological changes in LSMN.

This paper presents the results of electrochemical studies conducted with ethanol-fueled SOFCs as well as of physico-chemical characterization consisting of X-ray absorption characterization carried out on as-prepared, reduced, and tested LSMN, X-ray diffraction of the spent cell to demonstrate any possible carbon deposition, and SEM images to get insights into the morphology of the spent cell. The study is intended to demonstrate the feasibility of such an approach, in which real fuels can be used in solid oxide electrochemical cells, while maintaining a high interest in converting ethanol into power energy through an electrochemical process, which is intrinsically superior to what can be achieved with combustion engines.

2. Materials and methods

A nickel manganite of lanthanum and strontium mixed with ceria-doped gadolinia is used as a coating layer and will be referred to as LSMN-CGO electrocatalyst. LSMN was synthesised using pure metal nitrates to achieve a theoretical composition of $La_{1.5}Sr_{1.5}Mn_{1.5}Ni_{0.5}O_{7\pm\delta}$. Following initial thermal treatments at intermediate temperatures in air to burn off organic materials and remove residuals, followed by high temperatures processing to create a crystalline phase, this material exhibited a Ruddlesden-Popper structure with two rock-salt layers (RP n = 2). The detailed description of the synthesis procedure and the physico-chemical characterisation have been outlined in our previous paper [41].

Upon achieving the desired phase, the LSMN was mixed with $Ce_{0.1}Gd_{0.9}O_2$ (CGO) in a 70:30 wt ratio. This combination was chosen due to CGO's well-known ionic conductivity and oxygen spillover properties [68–70]. Consequently, the resulting electrocatalyst is expected to possess adequate ionic percolation and oxygen storage capacity, which could potentially enhance the oxidation of organic fuels. For adequate mixing of the ceramics (i.e., LSMN and CGO), 6 h of milling in ethanol was required to minimise friction in the jar.

Afterward, a slurry was prepared by mixing a 1:1 wt ratio of electrocatalyst powder (LSMN and CGO) to organics (5 wt% of binder (*i.e.*, Butvar) and 95 wt% of dispersant (*i.e.* α-terpineol) in ethanol for 2 h at 300 RPM. The resulting mixture was applied as a coating layer onto the anode side of an anode-supported SOFCMAN button cell (anode NiO + YSZ/400 μm, electrolyte YSZ/10–15 μm, barrier layer GDC/2–3 μm, cathode LSCF + GDC/20–25 μm) [71] obtained by laser-cutting from a large area cell. After curing at 1100 °C, the organics from the slurry were burned off, resulting in a strong adhesion between the coating layer and the SOFC Ni-based anode. In this experiment, the active area of the cell was 1.13 cm^2.

Subsequently, the button cell was mounted in the alumina reactor. The complete experimental setup for the test has been extensively detailed in our previous works [41,56,72,73]. Gold paste was painted as a grid and two gold wires for each electrode were used to connect the cell to external electrochemical testing equipment. Achieving a gas-tight seal for the anode compartment was accomplished using a ceramic paste (*e.g.* AREMCO) with specific curing steps, while the cathode side remained exposed to static air.

Upon reaching 700 °C, the anode compartment was purged with He (30 ml min^{-1}) and then supplied with diluted H_2 in He (50:50 vol) at a total flow rate of 60 ml min^{-1} and then in pure H_2 (60 ml min^{-1}) up to reaching a stable OCV. Once this step was concluded, the cell conditions were changed to bioethanol (90 vol% in H_2O) at a volumetric flow rate of 7.6 μl min^{-1} in liquid form, mirroring typical concentration values found in Brazilian ethanol stations [4] and consequently the cell was placed in operating conditions (i.e. circulating current density). The injection of bioethanol into the reactor was facilitated by a micropump attached to a strategically positioned nozzle for rapid vaporisation at suitable temperatures. Additionally, an inert carrier gas (He) was introduced at a rate of 2 ml min^{-1} to ensure uniform vapor distribution into the anodic chamber and efficient removal of the reaction products.

Electrochemical measurements were performed using a BioLogic instrument constituted by a booster up to 100 A and an impedance module ranging from ±10 V. Diagnostic procedures included galvanostatic durability testing, measurements of characteristic I-V curves achieved at a scan rate of 10 mV sec^{-1}, and impedance spectroscopy in the frequency range of 1 MHz–1 mHz with an amplitude of ±10 mV.

X-ray Absorption Spectroscopy (XAS) measurements were performed on the Ni-K and Mn-K edges of the as-prepared, reduced, and tested LSMN at the LISA-CRG beamline of the European Synchrotron [74]. The monochromator was equipped with a pair of Si(111) crystals cooled at Liquid Nitrogen temperature, whereas beam collimation, focusing and harmonic rejection were achieved by a pair of Si-coated mirrors (first cylindrical and second toroidal, E_{cutoff} = 15 keV). The incoming beam was monitored in a N_2-filled ion chamber; the beam size on the sample was about 100 * 100 μm^2. All measurements were carried out at room temperature. The "as-prepared" and "reduced" LSMN specimens were examined in transmission mode using a second ion chamber placed after the sample. The "tested" LSMN was measured on the remaining specimen attached to the electrode of the tested SOFC in Total Electron Yield (TEY) mode. This data collection mode allows a sampling depth below the sample surface of only a fraction of a micron [75]. These data were obtained in a Helium-filled chamber (P_{He} = 200 mbar) collecting the electrons with an anode placed at about 70 V with respect to the ground. Using this method, the signal contamination from Ni-YSZ electrode substrates is eliminated. In order to improve the signal-to-noise ratio, 2 to 8 spectra per sample were collected in each study case. In order to ensure the stability of the energy scale and provide a reliable calibration for determining the edge position, a reference foil was probed along with the samples. XAS data analysis was carried out using the IFEFFIT package for data reduction and fit [76], whereas the EXAFS (Extended X-ray Absorption Fine Structure) theoretical scattering paths were calculated with the FEFF8 code [77]. XANES (X-ray Absorption Near Edge Structure) and EXAFS parts were analysed, and the results are presented separately.

3. Results and discussions

A preliminary conditioning procedure was conducted with diluted H_2 and progressively switched to pure H_2 before the cell was put under operating conditions with liquid bioethanol at 90 % and He as a carrier. Fig. 1 shows the durability test carried out for 96 h during which, daily, the operation was stopped to conduct the diagnostic electrochemical characterization that will be discussed further in this paper. For this analysis, we started with a 50 mA cm^{-2} current density and gradually increased it to 400 mA cm^{-2} under galvanostatic conditions and recorded the cell potential accordingly. As shown in Fig. 1, in the period during which the current density was increased, the cell potential dropped, as expected, and this is a characteristic of fuel cells that lose voltage efficiency with increasing current drained from the cell. Further on, polarization curves are reported to illustrate this effect more clearly.

As can be seen from the trend of the cell potential up to at least the first stop of the cell and subsequent diagnostics, the cell's performance was partially lost once it was placed at 400 mA cm^{-2} on its first day of operation. This was the point when the cell appeared to become more stable, as a steady state condition had been achieved and persisted for about 96 h up to the end of the durability test. It was also evident that the cell behavior remained stable in spite of the interruptions for conducting redox cycles and Electrochemical Impedance Spectroscopy (EIS) experiments, as well as short periods of tens of minutes during which the

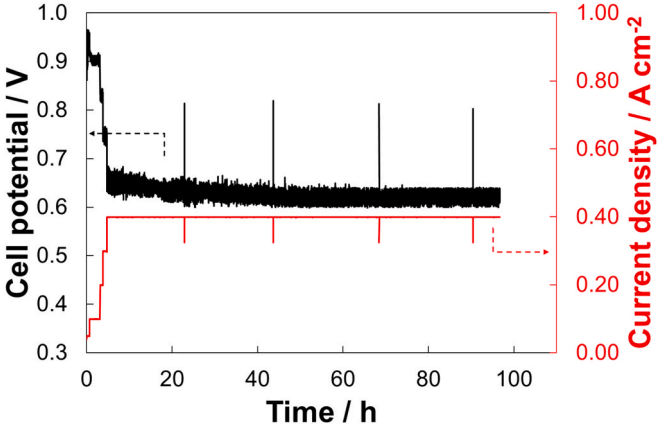

Fig. 1. Durability test carried out at 700 °C by feeding bioethanol at 90 vol% (7.6 μl min^{-1}) and He (2 ml min^{-1}) as carrier.

cell remained essentially at Open Circuit Voltage (OCV), during the EIS performed in this cell potential condition. Under OCV, not only there is not current circulation, but also H_2O cannot be generated at the anode and, as a consequence, steam reforming of fuel is suppressed. This makes OCV conditions the most stressful for a SOFC, leading to carbon deposits and fast cell degradation under these circumstances [78]. Therefore, the stable behavior observed immediately after the electrochemical diagnosis steps of the cell supports the hypothesis that the LSMN coating protects the cell from fuel cracking by mitigating its driving force.

Meanwhile, it was notable that the potential oscillated significantly, in an average range of 40 mV, throughout the entire durability test (Fig. 1). There are only a few possible explanations for this behaviour that is observed only in experiments using liquid fuels, while it was not seen in experiments using biogas [41,67]. The existence of this fact by itself excludes the possibility that this oscillation is the result of a reaction mechanism associated with fuel oxidation. As already discussed in our prior papers concerning similar architectures of cells having an anode coated with perovskites or derived from, the most likely complete fuel oxidation path can be described by the *shuttle mechanism* involving multiple reactions, each of which having its own kinetics and eventually producing intermediates [42]. Consequently, these oscillations could, in principle, be the result of fluctuating intermediate concentrations in the reaction zone (caused by factors such as diffusion, adsorption–desorption phenomena, and/or related chemical reactions), according to what has been reported in the literature [42], and involve multiple reactions as follows:

$$CH_3CH_2OH \xrightarrow{LSMN+CGO} -CH_{2_{ads}} + CO + 2H_2 \quad (1)$$

$$2H_2 + 2O^{2-} \xrightarrow{Ni-YSZ} 2H_2O + 4e^- \quad \text{(shuttle mechanism)} \quad (2)$$

$$H_2O + -CH_{2_{ads}} \xrightarrow{LSMN+CGO} 2H_2 + CO \quad (3)$$

$$2H_2 + 2O^{2-} \xrightarrow{Ni-YSZ} 2H_2O + 4e^- \quad (4)$$

$$2CO + 2O^{2-} \xrightarrow{Ni-YSZ} 2CO_2 + 4e^- \quad (5)$$

Therefore, the full ethanol oxidation half-cell reaction is as follows:

$$CH_3CH_2OH + 6O^{2-} \rightarrow 2CO_2 + 3H_2O + 12e^- \quad (6)$$

However, also intermediates can be formed as a result of chemical and electrochemical reactions, namely acetaldehyde, acetic acid, methane, and other C1 intermediates that increase the complexity of anode atmospheres, as well as the kinetics involved in their electrochemical conversion to CO_2 and H_2O.

An alternate explanation for the oscillation is linked to the pump used to feed liquid ethanol and the flow rate of He as a carrier. Based on our experience, the oscillation cannot be eliminated with our setup at all. Apparently, it is related to the pump's characteristics and the position of the ethanol injection nozzle within the reactor (*e.g.*, the cell is mounted at the edge of an alumina tube), where ethanol immediately evaporates and passes over the anode transported by He, creating a dense atmosphere over the SOFC's anode. Meanwhile, the flow rate of He greatly affected the cell's behavior. Possibly, ethanol vapor could not be efficiently carried to the anode's reactive zones with a relatively low flow of He. A relatively high flow rate, however, had the effect of depleting the region near the anode of fuel and its intermediates, in addition to negatively affecting the OCV's thermodynamics. With several tentative tests on similar cells, we reached a compromise with the flow set for this experiment. However, it is important to note that according to our best practices, the optimal conditions should be determined based on the measurement setup, cell dimensions, and fuel characteristics.

Fig. 2 shows the characteristic I-V curve obtained during the cell's preconditioning in H_2, along with the characteristic curves collected during its daily operation at 700 °C. Using H_2, the OCV was closed to 1.1 V, a typical value for cells ASC2 (2nd generation of anode-supported cells) operating at this temperature. Although this value is slightly lower than one reported by the cell manufacturer (Ni anode, without LSMN) [71], it appears to be in line with our measurements for the paper reporting the behaviour of this cell with biogas [72]. Therefore, the observed partial depletion of OCV compared to manufacturer's value was probably a consequence of different testing conditions, different flow rates, some shortcomings in our sealing method, or an effect of the coating layer, which could cause a small electronic leak. However, this OCV value remains still high, and the partial loss does not necessarily need to be considered as a constraint because, as can be seen from the

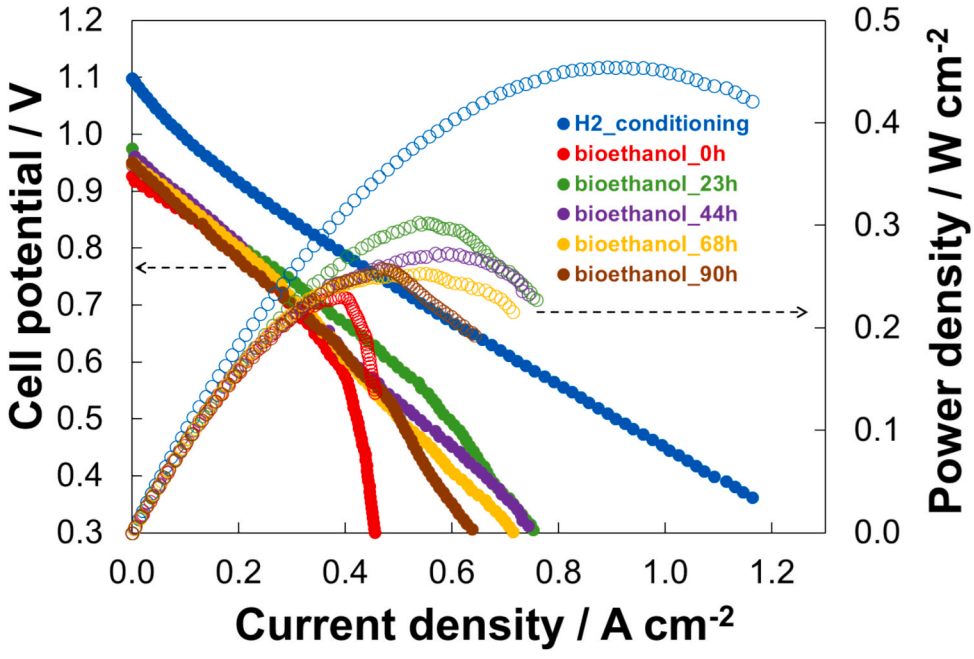

Fig. 2. Polarization curves measured daily on the coated SOFC operating at 700 °C.

manufacturers' curves, this value decays significantly immediately after a few milliamps of current are discharged.

In contrast, there is a much greater difference between our curves and those of the manufacturers in terms of curve features and total performance. We found that the maximum power density of the cell fed with H_2 was reduced by about 40 % compared with that of the manufacturer [71], mainly because of an increased I-V curve slope, probably caused by the coating layer added to the cell. As mentioned, LSMN used as a coating layer is derived from perovskites, which are generally less electronic conductors than nickel. Also, the coating layer thickness as well as the thermal treatment for achieving appropriate adhesion between the coating layer and the support, were not yet optimized and should be improved for better overall performance.

The focus of this study, however, was not to optimize this aspect but rather to demonstrate that a commercial cell which, in principle, cannot operate directly on carbon-based fuels due to Ni's significant limitations and cracking reactions as also demonstrated in one of our previous papers [42], can instead be operated in fuel-flexible mode by advancing knowledge about this cell configuration that has already been demonstrated with biogas [41,67].

When the fuel was moved to bioethanol, the initial OCV was around 0.94 V, and this value gradually increased throughout cell operation to reach a maximum value of 0.98 V. As it is expected, the *shuttle mechanism* of reactions generates many intermediates, so that the increase in voltage shall likely be a consequence of the raise of partial pressure of multiple intermediates, including H_2 and CO, that were initially absent or in a limited percentage, in the anode compartment. Although the gas composition at equilibrium can be predicted, this does not reflect the experiment's status since a cell placed under operating conditions would be very far from equilibrium, especially because ionic oxygen transported from the cathode through the electrolyte is more reactive than molecular oxygen.

Interesting features can be also observed from the polarization I-V curves (Fig. 2), obtained once the feed was switched to bioethanol. The curve obtained at 0 h appears to be controlled by a significant diffusion constraint, indicating a problem for the fuel to reach the triple phase boundary (TPB) rather than the release of products from the reactive zones. After 23 h, this effect was moved towards higher current density, which is consistent with the *shuttle mechanism*, which promotes a modification and thus simplification of fuel through multiple reactions involving dehydrogenation, partial oxidation, reforming, and finally resulting in a mixture of H_2 and CO. This mixture is able to diffuse quite smoothly through the anode and up to the region near the anode-electrolyte interface where TPB is wide. However, all of the I-V curves exhibited such a constraint at the higher current densities because the amount of fuel is insufficient to sustain cell operation under such conditions. In fact, the carrier percentage may play an important role in this constraint for at least two reasons. One is that using inert gas as a carrier dilutes the fuel. Secondly, because the carrier helps removing products far from the anode, but also the reagents present in the anode chamber in large excess. Thus, optimizing both the flow rates of bioethanol and N_2 as a carrier could improve the performance of the cell, and this may be a topic for further improvement.

For all tests involving bioethanol, a significant drop in cell potential was observed as a function of current density, but still remaining almost linear in the range between 0.9 V and 0.6 V, and with a slope that differed slightly from that observed in H_2. Therefore, from this point of view, it is obvious that a substantial part of the difference in performance achieved in bioethanol and H_2 is primarily a consequence of the relatively low OCV observed in bioethanol, compared to H_2, as well as the slightly higher ohmic resistance for bioethanol fed cells. However, a more detailed understanding of resistance differences can be gained by analysing EIS.

The impedance measurements at OCV are shown in Fig. 3 and some impedance parameters from the spectra are reported in Table 1. According to the polarization I-V curves, Fig. 2, the OCVs measured in bioethanol ranged from 0.94 to 0.98 Volts. This implies that the features of EIS spectra cannot be compared since their characteristics are largely dependent on the potential at which they are measured. However, there are some characteristics of these EIS spectra that can be discussed together.

According to Fig. 3 and Table 1, in the presence of H_2, the Rs (series resistance, measured as the X-axis intercept of Nyquist plot at high frequencies) was 0.28 O cm^2, significantly lower than the values observed with bioethanol. When using H_2, two semicircles are evident and the one at low frequency appears to be dominant. A typical characteristic of such a cell is that these semicircles are generally associated with the anodic and cathodic reactions, which at the OCV are mainly associated with the activation energy of the hydrogen oxidation and the oxygen reduction reactions [79,80]. As a general rule, for high-temperature cells, such as SOFCs, and for optimised cell architecture and materials, oxygen reduction is the most energetically intensive process [81]. Consequently, it is obvious that the high-frequency semicircle is associated with hydrogen oxidation and the low-frequency semicircle with oxygen reduction. In this case, however, we are facing with a coating layer that has not yet been well optimized in terms of morphology, composition, and adhesion to the anodic support, so the conclusion above may not be fully applicable. Nevertheless, it is interesting to note that the presence of a functional layer does not result in an additional semicircle or in a very high resistance constraint. When a layer is not sufficiently

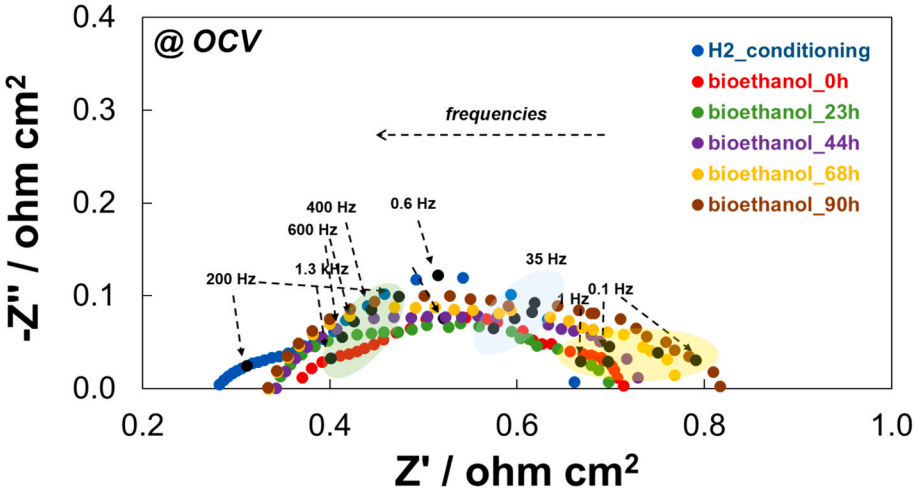

Fig. 3. EIS spectra measured at OCV and daily on the coated SOFC operating at 700 °C.

Table 1
The most significant electrochemical data obtained on the coated SOFC operating at 700 °C.

	OCV (Volts)	EIS @ OCV (Ohm cm^2)		EIS @ 800 mV (Ohm cm^2)		Power density @ 0.8 V (W cm^{-2})	Power density @ 0.7 V (W cm^{-2})
		Rs	*Rt*	*Rs*	*Rt*		
H_2 _conditioning	1.098	0.28	0.66	0.28	0.58	0.30	0.38
Bioethanol_0h	0.93	0.37	0.71	0.37	0.81	0.15	0.21
Bioethanol_23h	0.97	0.34	0.70	0.35	0.80	0.16	0.25
Bioethanol_44h	0.95	0.34	0.73	0.35	0.82	0.16	0.22
Bioethanol_68h	0.95	0.33	0.77	0.34	0.92	0.16	0.22
Bioethanol_90h	0.95	0.33	0.82	0.34	0.91	0.14	0.21

conductive, such as metals supported on ceramics, usually used as catalysts for fuel reforming, current circulation is difficult, making the operation of SOFCs very challenging. Therefore, in our cell architecture, there is no dramatic increase in cell internal resistance that would render the cell unusable, and although the coating layer adds some resistance, it is not significant.

When bioethanol was fed to the cell, a minor reducing atmosphere resulted in an immediate increase of Rs to 0.37 O cm^2 (Table 1), which is about 0.1 O cm^2 higher than that caused by H_2. Yet, there is also a possibility that this increase is a consequence of partial Ni re-oxidation, primarily due to the presence of H_2O in the feed of ethanol (10 %). As a result of prolonged exposure to ethanol, the Rs decreases to 0.33 O cm^2, suggesting that the reducing force of the environment in the anode compartment is altered. As discussed above, the *shuttle mechanism* could be responsible for this change because it is expected to promote a modification of the gas compositions into anodic compartments due to ethanol decomposition into intermediates like H_2 and CO, creating a different atmosphere in the anode compartment than the initial one. As mentioned above, a notable feature of the EIS spectra measured for the cell fed with bioethanol is their higher Rs compared to that fed with H_2. In theory, carbon deposits in the anode as a result of carbon-containing fuel cracking promote an increase in electronic percolation in the anode, and one effect on EIS is the reduction of Rs. In addition, fuel oxidation generally becomes more challenging [82–84]. This is because anodic pores are occluded, so that the Triple Phase Boundary (TPB) extension is reduced, resulting in increased constraints on turnover events. Furthermore, the occlusion of pores increases the diffusion constraints for reactants and products [85]. Generally, all of these effects would be seen in the EIS spectrum by a slight decrease in Rs but a rapid increase in the total resistance (Rt, the intercept of EIS with x-axis at low frequencies). Interestingly, none of these features changed in the EIS of bioethanol-fed cells during the entire period of this testing (Tabel 1), proving the effectiveness of the electrochemical anodic process occurring in the LSMN protecting layer.

In contrast to pure H_2, in the EIS measured for bioethanol-fed cells, a third semicircle can also be seen. Based on previous experience with similar cell architectures, we believe that such behavior occurs when multiple oxidizable species are present at the same time, including H_2 and CO, which exhibit similar kinetics [73,78,86]. For example, carboxylic acids and aldehydes that are intermediates produced during the partial oxidation of bioethanol, as well as unconverted ethanol, can be oxidized by different mechanisms and at different rates. Consequently, these species will diffuse to the cell's region where TPB is relatively abundant and will react with ionic oxygen, each with a specific kinetics and number of electrons involved. Therefore, some of the heavy species could contribute to one semicircle of the EIS. Frequencies for each individual semicircle suggest evidence of this effect. According to the experiment conducted at OCV with H_2, the high frequency semicircle is centered around 200 Hz and the low frequency semicircle is centered around 0.6 Hz. Upon switching to bioethanol, the high frequency semicircle appears around 1.3 kHz and then moves to 200 Hz after 90 h, achieving the same value as H_2. A 35 Hz intermediate semicircle is observed, while the slower mechanism is between 1 and 0.1 Hz, similar to the slower mechanism found in cells fed with H_2. Thus, the additional semicircle observed for experiments conducted with bioethanol is the medium-frequency semicircle, which may reflect the oxidation of heavy intermediates.

Fig. 4 and Table 1 show the EIS data obtained at a cell voltage of 800 mV. During these analyses, it was observed that feeding H_2 resulted in almost the same Rs as at OCV, while Rt decreased. It is a general effect of voltage at which EIS measurements are carried out, and it is also evident in the shape of the I-V curves (Fig. 2) where an apparent change in slope is visible around 1 V for the experiment carried out in H_2. At 800 mV, the slope of the I-V curve for the H_2-fed cell was slightly lower than that observed at OCV, supporting a more effective electrochemical process. In addition, as illustrated in Fig. 3, the EIS of the H_2-fed cell still exhibits two semicircles at 800 mV and most significant changes are observed at low frequencies. It is basically a matter of the more energetic process becoming more effective with the increase in current density, as happened at 800 mV. For an optimised cell operating in H_2 and air, this phenomenon correlates with the reduction of molecular oxygen, which is more energy-intensive and requires twice the electrons of molecular hydrogen oxidation.

In contrast, the cell fed with bioethanol exhibits a different behavior. This experiment shows a relatively low OCV, below 1 V, during the durability test, and the slope at low current density does not correlate with a strong activation energy. However, at 800 mV the curves for bioethanol show a worse slope feature compared to OCV. Therefore, the EIS of Fig. 4 shows a higher Rt than the related spectrum recorded at OCV (Fig. 3). Additionally, these EIS showed at least three-four semicircles. This aspect is discussed in the Supplementary Materials through an analysis of the relaxation time distribution based on the fitted EIS at 800 mV. They also appeared quite noisy due to the oscillation caused by the pump, as we have already discussed for the durability test in Fig. 1. In spite of this, it was quite evident that the EIS behaved similarly to that of OCV (Fig. 3). Initially, the Rs value was 0.37 O cm^2, but it decreased to 0.34 O cm^2 as testing time passed. In contrast, there was a progressive increase in Rt, which at the end of the durability test (90 h), reached approximately 0.91 O cm^2. Of course, this significant resistance was responsible for the overall performance of the cell. A further insight is gained by considering the frequencies of each semicircle recognized at 800 mV. Across all experiments, the fastest semicircle is around 1.3 kHz, which suggests similar kinetics in experiments involving H_2 and bioethanol, since this fuel is expected to be simplified to syngas and other intermediates according to the shuttle mechanism. Across all experiments, medium frequency semicircles are centered around 5 Hz and suggest a similar mechanism likely related to oxygen reduction. Additionally, only ethanol experiments have low-frequency semicircles around 0.01–0.14 Hz, indicative of a more kinetically constrained mechanism probably related to the oxidation of heavy intermediates.

In Table 1, we present a comprehensive report of the major findings of this cell diagnosis.

A comparison of XRD spectra of LSMN after it is calcined at 1100 °C, after its reduction at 800 °C, and as a coating layer of the spent cell is shown in Fig. 5. As a result of this study, it is evident that the grazing angle of the cell hinders the identification of LSMN's exact state in the

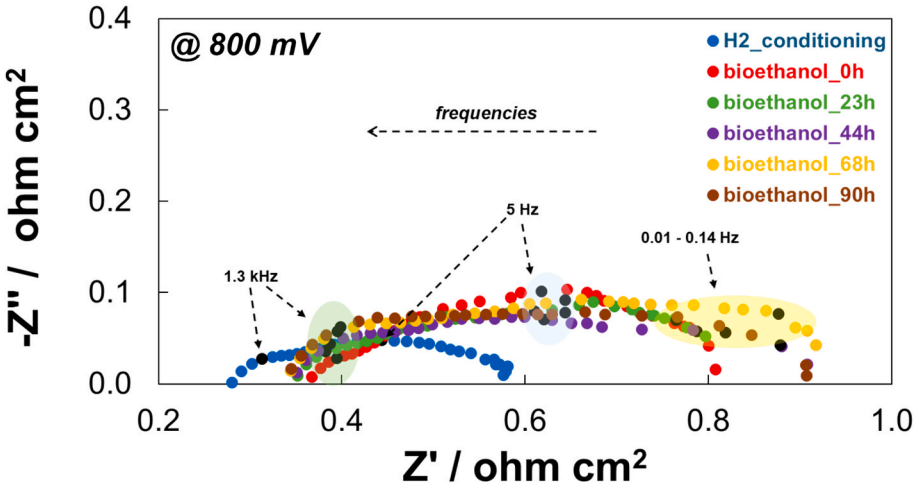

Fig. 4. EIS spectra measured at 800 mV and daily on the coated SOFC operating at 700 °C.

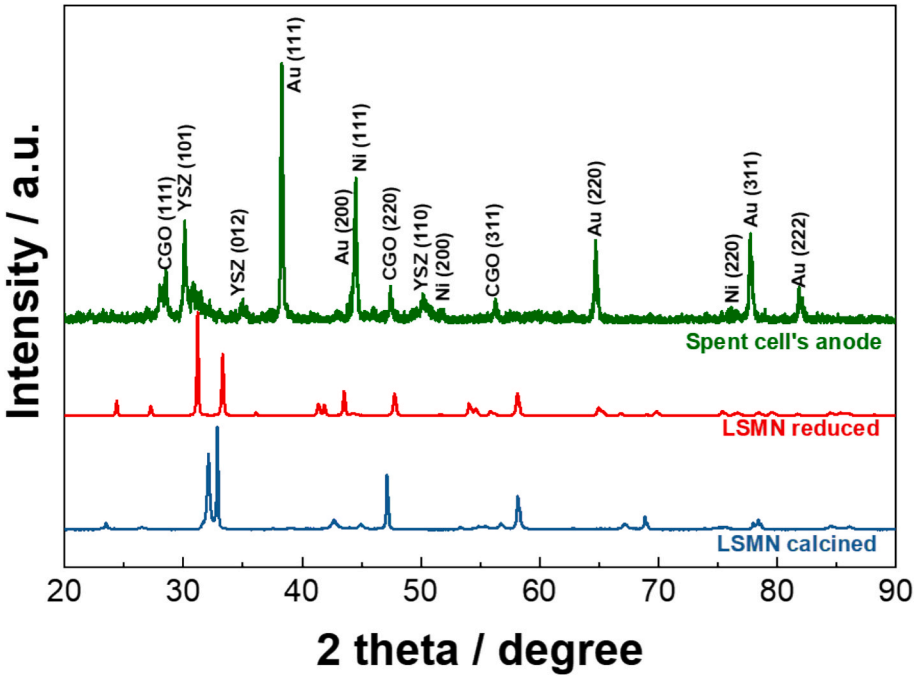

Fig. 5. Patterns of LSMN after calcination at 1100 °C accomplished during the synthesis procedure, subsequent reduction at 800 °C simulating operating conditions, and as a coating layer as a result of prolonged cell operation.

coating layer. There are multiple reflections due to the support (i.e. metallic Ni (JCPDS card 04-0850) and YSZ (JCPDS card 37-1307), reflections of Au (JCPDS card 04-0784) derived from the gold paste used for the electrical contacts, and reflections of CGO (JCPDS card of CeO_2 04-0593) used in mixture with LSMN to enhance oxygen spillover characteristics and oxygen ion percolation within the coating layer. According to this figure, the support is in a reduced state because no NiO patterns were observed (JCPDS 04-0835 or 22-1189) and, perhaps more interestingly, there was no clear signal indicative of carbon, which generally appears broad around 26.65° because it is amorphous when formed as a result of cocking.

In Fig. 6, morphology of fresh bare and spent cells is analyzed by SEM. It is apparent from the freshly bare cell that the Ni-YSZ support is oxidized, which results in a limited porosity at the anode. This photo shows the electrolyte (i.e. YSZ), which appears to be dense with a thickness of about 10 μm, the barrier layer (i.e. CGO, about 2.8 μm) which protects the cathode from direct contact with the main electrolyte and is a bit thinner than the main electrolyte, and a porous cathode.

In contrast, the used cell exhibited a reduced anode with a more "open" morphology. In this case, YSZ particles measuring 0.9–1.7 mm and Ni particles of finer size can clearly be seen. There is a noticeable difference in the coating layer morphology (about 33 μm), as well as a regular interface between the coating layer and the supporting anode. Carbon is not evidently present in either the anode or coating layer, which confirms the other experimental findings.

XANES data provided semi-quantitative information about the valence state of the metals under analysis, Mn and Ni in the present case and revealed the chemical evolution of these elements in consequence of chemical and electrochemical reactions. Fig. 7 shows on the left side the data at the Mn-K edge compared with reference compounds for Mn^{4+} (MnO_2), Mn^{3+} (Mn_2O_3, bixbyite), and Mn^{2+} (MnO) taken from the LISA beamline database [87]. The as-prepared sample exhibited an edge coinciding with that of MnO_2, confirming its valence state near 4+, as expected for the perovskite structure. In the reduced sample, an edge

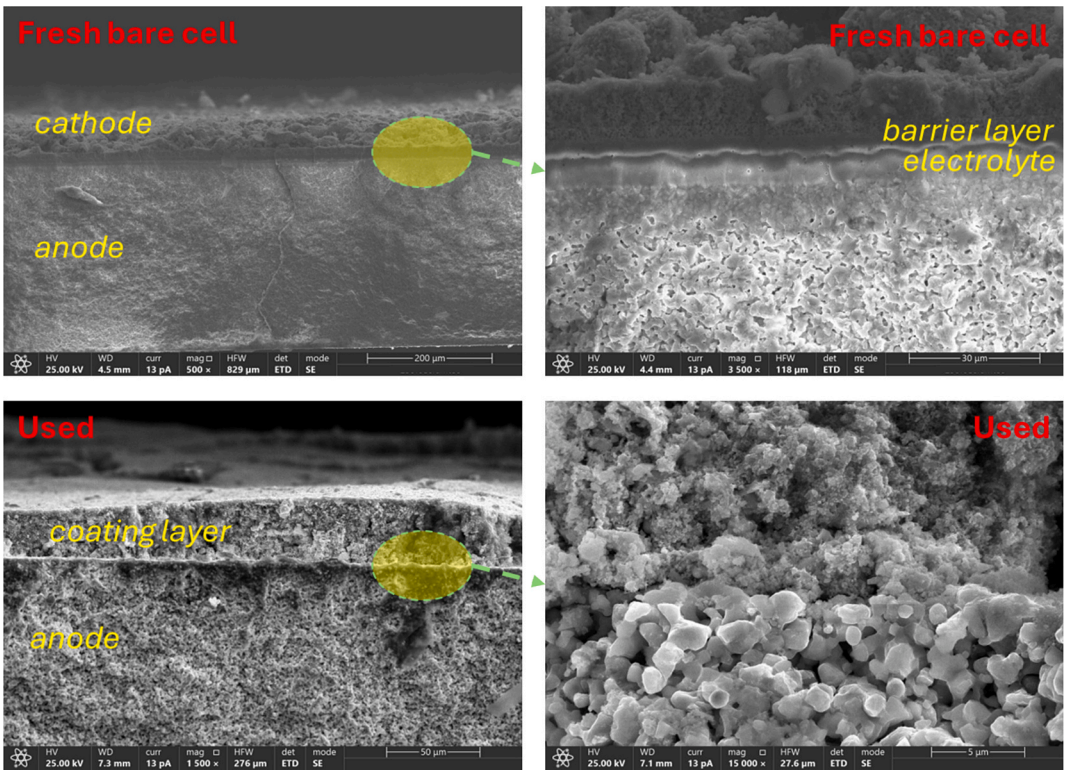

Fig. 6. Study illustrating the layers of bare and spent cells by SEM.

appears at the same position as the Mn in bixbyite, indicating a 3+ valence state. Meanwhile, the tested sample is positioned halfway between MnO and Mn_2O_3, revealing a valence state between 2+ and 3+ . Concerning Mn in the spent material the XAS analysis shows a valence shift for Mn and a structural increased disorder. However, the data are still compatible with a perovskite model (i.e. oxygen in the first coordination shell and a mix of La/Sr in the second shell) so it is reasonable to suppose that the RP phase adapts to the modified valence of Mn though maintaining the perovskite structure. In this case, lacking appropriate reference compounds, it is not possible to perform the Linear Combination Fitting (LCF) analysis of the XANES part.

In the case of Ni (Fig. 7, right), its edge raises at an energy slightly above that of the model compound NiO, revealing a valence state above 2+ for Ni. When reduced, metallic Ni forms, as evidenced by a marked edge shift to lower energies so that the spectrum coincides with that of the metal. Following electrochemical cycles, the tested sample exhibits an edge still close to that of the metal. Nevertheless, the presence of a slight white line at about 8350 eV suggests the co-presence of an oxide phase. According to the EXAFS analysis (Fig. 8), however, this oxidation is of a limited amount, passing from 0.9(1) to 0.8(1). This observation is confirmed by the XANES analysis made by LCF analysis using metal and NiO as models.

Quantitative EXAFS analysis has been carried out using the ARTEMIS code [76], and for the fitting procedure, the theoretical EXAFS signals were derived using the FEFF8 code [77] based on the structure of a mixed La/Se perovskite $(La_{1.2}Sr_{0.8})MnO_{3.94}$ [88]. As analogous literature data for Ni were not available, in order to analyse the data at the Ni edge, this metal was substituted for Mn in the previous structure [88].

Fig. 8 shows the results from the analysis of the samples at both the Mn-K and Ni-K edges. In this analysis, a three-shell model was fitted to the data: a metal (either Ni or Mn)-Oxygen shell (visible on the Fourier Transform –FT- as a peak at about 1.5 Å), a mixed metal-La/Sr shell, (peak at 2.6 Å in the FT) and a Metal-Oxygen-Metal (collinear configuration visible at about 3.5 Å in the FT) shell. Note that the FT presented here are not phase-corrected, so the peaks do not appear exactly at the crystallographic values. Table 2 summarizes the quantitative results of these analyses. A Mn-O excess of 30 % was detected, which indicates that not all the metal is in its perovskite form, rather it is competing in an amorphous oxide phase. In the coordination shells above the first, the crystallographic values of neighbors were taken into account. The La/Sr ratio was also fitted in these analyses, yielding a value of 0.50(5). In the as-prepared sample the perovskite structure can well reproduce the data with the 3 coordination shells, confirming the occurrence of this phase in this sample.

Upon sample reduction, a different behavior is observed for the two metals. Mn keeps a perovskite-like structure, as testified by the three coordination shells still well visible in the Fourier Transform, with some rearrangement with respect to the pristine structure. Most presumably, the cations of the A site move from the perovskite layer of the RP phase to the rock-salt layer to balance the charge change occurring in the B site with the loss of Ni and the valence change of Mn. On the other hand, Ni exsolves from the perovskite forming metal particles, as confirmed by the fit extended up to 4 coordination shells.

Concerning the tested material, in the case of Mn, the structure was heavily disordered compared with the reduced material, nonetheless, a perovskite-like model can still reproduce the data. This can be explained by the fact that as Mn changes its valence state, so changing its ionic radius, a change in the La/Sr ratio should take place (although not detectable by the EXAFS data), resulting in an evolution of the RP phase and altered coordination distances.

In contrast, nickel (Table 3) still fits on four coordination shells in the *fcc* structure, although with a slightly reduced metallic fraction that can tentatively be explained by the presence of a minority oxide phase, as also suggested by the XANES spectrum.

A relatively high cell potential coupled with an excess of fuel resulted in the cell being operated under a reversible mode, and as a result, the anode operated under acceptable reducing conditions. It is not surprising that this result occurs since water and CO_2 are formed during operation, promoting a slight re-oxidation of Ni, especially at the surface level.

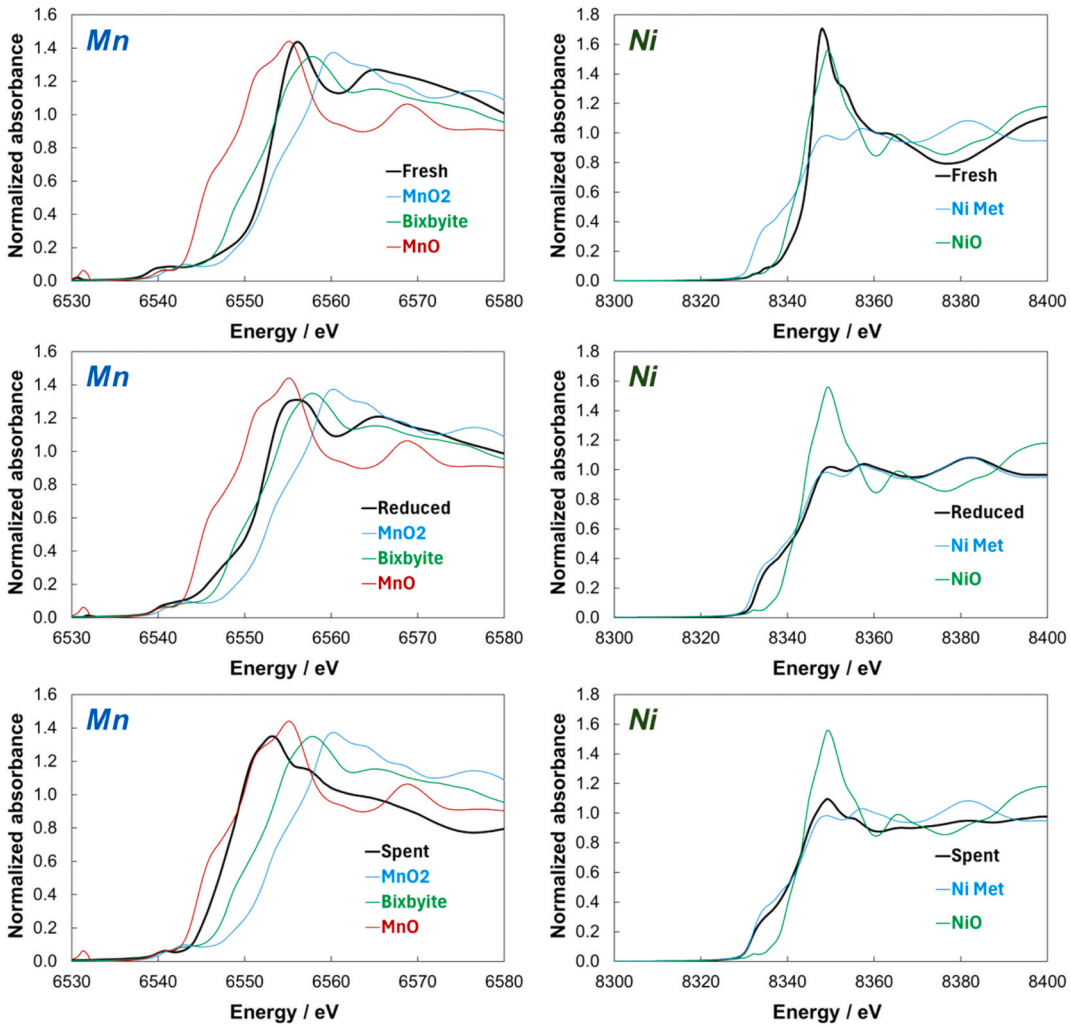

Fig. 7. XANES at the Mn-K edge (Left) and Ni-K edge (Right) for the as-prepared (top), reduced (centre), and tested (bottom) electrodes. Spectra are compared with model compounds [87]: MnO, Bixbyite (Mn_2O_3), MnO_2, NiO, and metallic Ni.

4. Conclusions

This study reports the results obtained with a commercial SOFC coated with a novel exsolved perovskite layer (i.e., LSMN) and fed with ethanol at a volume percentage commonly found in Brazilian fuel stations. The goal was to show that this approach could overcome limitations associated with commercial cells for stationary applications while improving the realistic utilization of these devices in place of conventional combustion engines. In order to prove this, electrochemical tests were conducted, showing the cell's stability for a long period (approx. 100 h) in an operational mode where commercial cells usually decay rapidly with this fuel. Additionally, the detailed electrochemical analysis (*e.g.*, polarization curves and impedance spectra) proved that one of the key factors in the success of this approach is the modification of the fuel over the coating layer leading to substantial contribution to suppressing carbon deposition in the Ni-reach layer. In a few of our previous papers, it was discussed and studied the *shuttle mechanism* that enabled this behavior. According to the I-V curves, a maximum power density of 300 mW cm^{-2} @ 0.57 V was achieved when diffusion constraints were mitigated by simplification of the fuel, as expected when considering the *shuttle mechanism* as the effective event occurring in the LSMN layer during operation. There were also two kinetics for the oxidation mechanisms occurring on the anode in the EIS analyses, which is a further indication that the anode chamber was subjected to a complex fuel atmosphere. Bulk analysis of as-prepared, reduced, and tested LSMN-based specimens has revealed that the initial structure of perovskites observed in the as-prepared material is lost after reduction in favour of a Ruddlesden-Popper phase, as indicated by Ni signals associated with its metallic phase, and Mn signals associated with the Mn^{3+} phase. These results indicate that despite being exposed to H_2O and CO_2 produced by the ethanol conversion into electricity and the H_2O being fed in solution with ethanol (10 vol%), the electrocatalyst remained under reducing conditions, preventing extensive LSMN reoxidation.

CRediT authorship contribution statement

F.Matos de Oliveira: Writing – original draft, Investigation, Data curation. **S. Vecino-Mantilla:** Validation, Supervision, Investigation, Data curation. **Z. Hafsi:** Supervision, Software, Investigation, Data curation. **M.V. Barp:** Writing – original draft, Validation, Software, Data curation. **F. D'Acapito:** Writing – original draft, Supervision, Methodology, Data curation, Conceptualization. **A. Puri:** Visualization, Software, Formal analysis. **J. Perez:** Supervision, Methodology, Investigation. **E. Ticianelli:** Writing – review & editing, Supervision, Resources. **M.Lo Faro:** Writing – review & editing, Supervision, Resources, Project administration, Methodology, Funding acquisition, Conceptualization.

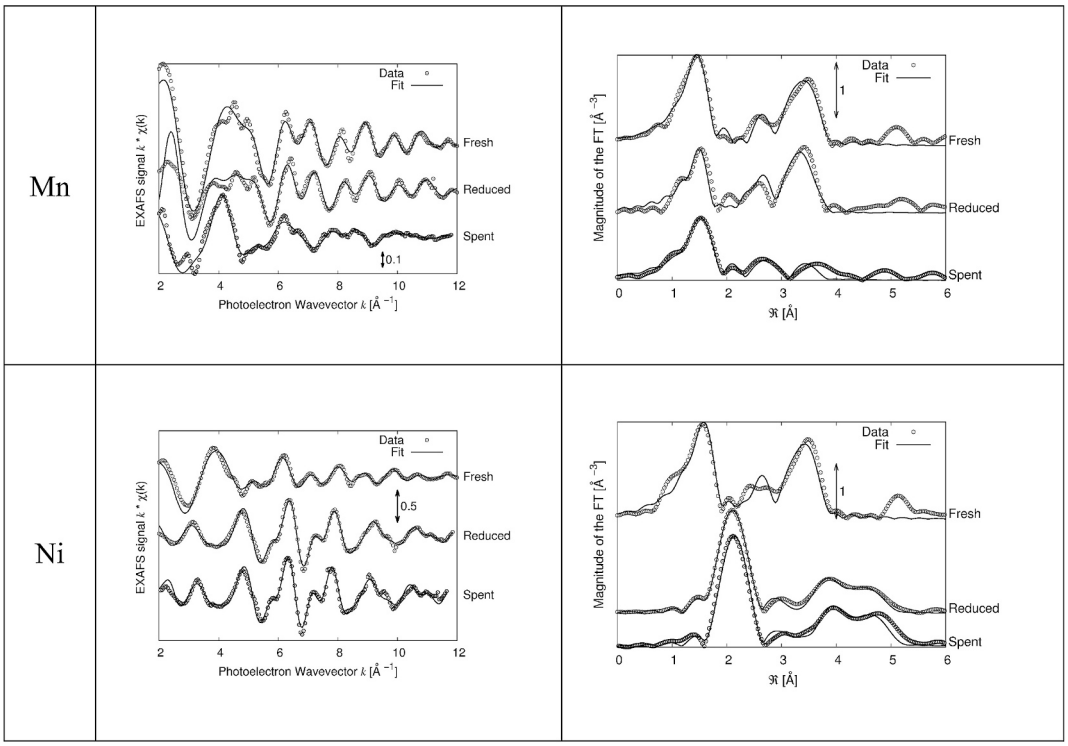

Fig. 8. Spectra of samples at both the Mn-K and Ni-K edges compared with the related best fits. Fourier Transforms were taken from k^2 weighted spectra using a Hanning window (apodization $\Delta k = 0.5$ Å^{-1}) with limits k = 3–12 Å^{-1}.

Table 2
Results of EXAFS analyses performed on the samples bearing the perovskite structure. Mn samples and the as-prepared Ni sample.

Sample	R_{met-O} (A)	σ^2_{met-O} (A^2)	$R_{met-La/Sr}$ (A)	$\sigma^2_{met-La/Sr}$ (A^2)	$R_{met-met}$ (A)	$\sigma^2_{met-met}$ (A^2)
Ref [88]	1.91*4 2.27*2		3.29 *8		3.83 *4	
Mn as-prepared	1.87(1)	0.003(1)	3.27(2)	0.002(1)	3.84(2)	0.003(1)
Mn reduced	1.87(2)	0.002 (2)	3.32	0.011(1)	3.77	0.013 (1)
Mn tested	1.99(4)	0.002 (2)	3.1 (1) La3.2 (1) Sr	0.009(1)	–	–
Ni as-prepared	2.01(2)	0.004(2)	3.27(2)	0.004(2)	3.85(2)	0.005(2)

Table 3
Results of the quantitative EXAFS analysis of the reduced and tested samples at the Ni-K edge. The structure was fitted with 4 coordination shells with distances derived from an overall lattice parameter value. For clarity, the structural values for the first shell are also reported. The global amplitude was calibrated on a metallic Ni model and found to be slightly reduced in the tested sample, suggesting the presence of an oxide phase.

Sample	Metal Fraction	latt. Par *a* (Å)	R_{Ni-Ni} (Å)	s^2_{Ni-Ni} (A^2)
Ni reduced	0.9(1)	3.54(1)	2.49(1)	0.006(1)
Ni tested	0.8(1)	3.53(1)	2.48(1)	0.005(1)

Declaration of competing interest

The authors declare that they have no known competing financial interests or personal relationships that could have appeared to influence the work reported in this paper.

Acknowledgments

This research was funded by the European Union – NextGeneration EU from the Italian Ministry of Environment and Energy Security POR H2 AdP MMES/ENEA with involvement of CNR and Ricerca sul Sistema Energetico (RSE), PNRR - Mission 2, Component 2, Investment 3.5 "Ricerca e sviluppo sull'idrogeno", CUP: B93C22000630006.

In addition, the authors acknowledge the Italian Ministry of University and Research (MUR) for funding the PRIN project SUPERH2, CUPE53D23009400006 and PRIN PNRR project OxCellenT, CUP B53D23027440001.

Dr. Hafsi acknowledges the ITELECTROLAB, the Joint lab between CNR-ITAE and IQSC-USP financed by the National Research Council of Italy (CNR)

F. Matos de Oliveira acknowledges CNPq for financial support (402209/2022-2) (200282/2023-9).

Dr. Lo Faro and IQSC-USP authors acknowledge the bilateral project "FlexPower- Solid Oxide Fuel Cell fed with Biofuel as an Electric FlexibleProvider in a Distributed Grid" granted by Italian Ministry of Foreign Affairs and International Cooperation - Brazilian National Council for State Funding Agencies (MAECI-CONFAP) Proc. 2020/00610-7.

IQSC-USP authors thank the Fapesp/Shell project Proc 2020/15230-5 - BG E&P Brasil (Shell)-CPE "Research Centre for Greenhouse Gas Innovation - RCG2I".

D'Acapito and Puri acknowledge the beamline LISA is a project funded by the Consiglio Nazionale delle Ricerche (project DFM. AD006.072). The data at LISA were collected under the In House Research program during experiments IHMA467 and IHMA473 and possess respectively the DOI: 10.15151/ESRF-ES-1570494939 and 10.15151/ESRF-ES-1587407526.

Appendix A. Supplementary data

Supplementary data to this article can be found online at https://doi.org/10.1016/j.cej.2025.162981.

Data availability

Data will be made available on request.

References

[1] J.P. Holdren, Population and the energy problem, Popul. Environ. 12 (1991) 231–255.
[2] IEA. IEA (2024), Electricity 2024. (2024).
[3] IEA. IEA (2023), We can't defeat climate change by investing in a handful of countries. The world needs to come together at COP28 – and fund a just energy transition. (2023).
[4] M. Lo Faro, D.A. Cantane, F. Naro, In the path for creating Research-to-business new opportunities on green hydrogen between Italy and Brazil, Int. J. Hydrogen Energy 48 (2023) 11876–11884.
[5] O. Yamamoto, Solid oxide fuel cells: fundamental aspects and prospects, Electrochim. Acta 45 (2000) 2423–2435.
[6] S.C. Singhal, Advances in solid oxide fuel cell technology, Solid State Ion. 135 (2000) 305–313.
[7] K.W. Bedringås, I.S. Ertesvåg, S. Byggstøyl, B.F. Magnussen, Exergy analysis of solid-oxide fuel-cell (SOFC) systems, Energy 22 (1997) 403–412.
[8] M. Dokiya, SOFC system and technology, Solid State Ion. 152–153 (2002) 383–392.
[9] P. Holtappels, U. Stimming, Solid oxide fuel cells (SOFC): John Wiley & Sons, Ltd, (2010).
[10] L. Merfort, N. Bauer, F. Humpenöder, D. Klein, J. Strefler, A. Popp, et al., Bioenergy-induced land-use-change emissions with sectorally fragmented policies, Nat. Clim. Chang. 13 (2023) 685–692.
[11] E.B. Sydney, L.A.J. Letti, S.G. Karp, A.C.N. Sydney, L.P.S. Vandenberghe, J.C. de Carvalho, et al., Current analysis and future perspective of reduction in worldwide greenhouse gases emissions by using first and second generation bioethanol in the transportation sector, Bioresour. Technol. Rep. 7 (2019) 100234.
[12] J. Li, F. Xiong, M. Fan, Z. Chen, The role of nonfood bioethanol production in neutralizing China's transport carbon emissions: An integrated life cycle environmental-economic assessment, Energy Sustain. Dev. 70 (2022) 68–77.
[13] M.H. Nguyen, R.G.H. Prince, A simple rule for bioenergy conversion plant size optimisation: Bioethanol from sugar cane and sweet sorghum, Biomass Bioenergy 10 (1996) 361–365.
[14] C.E. Wyman, Biomass ethanol: Technical progress, opportunities, and commercial challenges, Annu. Rev. Energy Env. 24 (1999) 189–226.
[15] P. Tsiakaras, A. Demin, Thermodynamic analysis of a solid oxide fuel cell system fuelled by ethanol, J. Power Sources 102 (2001) 210–217.
[16] S.L. Douvartzides, F.A. Coutelieris, A.K. Demin, P.E. Tsiakaras, Fuel options for solid oxide fuel cells: A thermodynamic analysis, AIChE J 49 (2003) 248–257.
[17] S.L. Douvartzides, F.A. Coutelieris, P.E. Tsiakaras, On the systematic optimization of ethanol fed SOFC-based electricity generating systems in terms of energy and exergy, J. Power Sources 114 (2003) 203–212.
[18] M. Cimenti, J.M. Hill, Thermodynamic analysis of solid oxide fuel cells operated with methanol and ethanol under direct utilization, steam reforming, dry reforming or partial oxidation conditions, J. Power Sources 186 (2009) 377–384.
[19] N.D. Neto, E. Heiss, From outsider to world leader: Bioethanol in Brazil. Low Carbon Development: Key Issues2013, 284-96.
[20] A. Walter, P. Dolzan, O. Quilodrán, J.G. de Oliveira, C. da Silva, F. Piacente, et al., Sustainability assessment of bio-ethanol production in Brazil considering land use change, GHG emissions and socio-economic aspects, Energy Policy 39 (2011) 5703–5716.
[21] H.V. Amorim, M.L. Lopes, J.V. De Castro Oliveira, M.S. Buckeridge, G.H. Goldman, Scientific challenges of bioethanol production in Brazil, Appl. Microbiol. Biotechnol. 91 (2011) 1267–1275.
[22] L. Hernández, V. Kafarov, Use of bioethanol for sustainable electrical energy production, Int. J. Hydrogen Energy 34 (2009) 7041–7050.
[23] A. Demirbas, Progress and recent trends in biofuels, Prog. Energy Combust. Sci. 33 (2007) 1–18.
[24] G.J. Offer, J. Mermelstein, E. Brightman, N.P. Brandon, Thermodynamics and kinetics of the interaction of carbon and sulfur with solid oxide fuel cell anodes, J. Am. Ceram. Soc. 92 (2009) 763–780.
[25] S. Zha, Z. Cheng, M. Liu, Sulfur poisoning and regeneration of ni-based anodes in solid oxide fuel cells, J. Electrochem. Soc. 154 (2007) B201–B206.
[26] P. Marocco, M. Gandiglio, M. Santarelli, When SOFC-based cogeneration systems become convenient? A cost-optimal analysis, Energy Rep. 8 (2022) 8709–8721.
[27] S. Santhanam, D. Ullmer, Z. Wuillemin, E. Varkaraki, C. Beetschen, Y. Antonetti, et al. Experimental analysis of a 25 kWe solid oxide fuel cell module for co-generation of hydrogen and power. ECS Transactions, 1 ed2019 159-66.
[28] G.J. Nelson, K.N. Grew, J.R. Izzo Jr, J.J. Lombardo, W.M. Harris, A. Faes, et al., Three-dimensional microstructural changes in the Ni-YSZ solid oxide fuel cell anode during operation, Acta Mater. 60 (2012) 3491–3500.
[29] O.M. Pecho, A. Mai, B. Münch, T. Hocker, R.J. Flatt, L. Holzer, 3D microstructure effects in Ni-YSZ anodes: Influence of TPB lengths on the electrochemical performance, Materials 8 (2015) 7129–7144.
[30] H. Tu, U. Stimming, Advances, aging mechanisms and lifetime in solid-oxide fuel cells, J. Power Sources 127 (2004) 284–293.
[31] J. Udagawa, P. Aguiar, N.P. Brandon, Hydrogen production through steam electrolysis: Model-based steady state performance of a cathode-supported intermediate temperature solid oxide electrolysis cell, J. Power Sources 166 (2007) 127–136.
[32] A. Brisse, J. Schefold, M. Zahid, High temperature water electrolysis in solid oxide cells, Int. J. Hydrogen Energy 33 (2008) 5375–5382.
[33] M. Lo Faro, S.C. Zignani, S. Trocino, V. Antonucci, A.S. Aricò, New insights on the co-electrolysis of CO_2 and H_2O through a solid oxide electrolyser operating at intermediate temperatures, Electrochim. Acta 296 (2019) 458–464.
[34] J. Nielsen, T. Jacobsen, Three-phase-boundary dynamics at metal/YSZ microelectrodes, Solid State Ion. 178 (2008) 1769–1776.
[35] D. Montinaro, V.M. Sglavo, M. Bertoldi, T. Zandonella, A. Aricò, M. Lo Faro, et al., Tape casting fabrication and co-sintering of solid oxide "half cells" with a cathode–electrolyte porous interface, Solid State Ion. 177 (2006) 2093–2097.
[36] M.S. Khan, S.-B. Lee, R.-H. Song, J.-W. Lee, T.-H. Lim, S.-J. Park, Fundamental mechanisms involved in the degradation of nickel–yttria stabilized zirconia (Ni–YSZ) anode during solid oxide fuel cells operation: A review, Ceram. Int. 42 (2016) 35–48.
[37] D. Singh, E. Hernández-Pacheco, P.N. Hutton, N. Patel, M.D. Mann, Carbon deposition in an SOFC fueled by tar-laden biomass gas: a thermodynamic analysis, J. Power Sources 142 (2005) 194–199.
[38] T. Iida, M. Kawano, T. Matsui, R. Kikuchi, K. Eguchi, Internal reforming of SOFCs: carbon deposition on fuel electrode and subsequent deterioration of cell, J. Electrochem. Soc. 154 (2007) B234–B241.
[39] S.A. Barnett, Direct hydrocarbon SOFCs: John Wiley & Sons, Ltd; 2010.
[40] C. Schluckner, V. Subotić, V. Lawlor, C. Hochenauer, Carbon deposition simulation in porous SOFC anodes: a detailed numerical analysis of major carbon precursors, J. Fuel Cell Sci. Technol. 12 (2015).
[41] S. Vecino-Mantilla, S.C. Zignani, R.-N. Vannier, A.S. Aricò, F.M. Lo, Insights on a Ruddlesden-Popper phase as an active layer for a solid oxide fuel cell fed with dry biogas, Renew. Energy 192 (2022) 784–792.
[42] M. Lo Faro, R.M. Reis, G.G.A. Saglietti, V.L. Oliveira, S.C. Zignani, S. Trocino, et al., Solid oxide fuel cells fed with dry ethanol: The effect of a perovskite protective anodic layer containing dispersed Ni-alloy @ FeOx core-shell nanoparticles, Appl. Catal. B: Environ. 220 (2018) 98–110.
[43] P. Zhang, L. Hu, B. Zhao, Z. Lei, B. Ge, Z. Yang, et al., Direct power generation from ethanol by solid oxide fuel cells with an integrated catalyst layer, Fuel 333 (2023) 126340.
[44] J.P.P. Huijsmans, F.P.F. Van Berkel, G.M. Christie, Intermediate temperature SOFC - A promise for the 21st century, J. Power Sources 71 (1998) 107–110.
[45] D.J.L. Brett, A. Atkinson, N.P. Brandon, S.J. Skinner, Intermediate temperature solid oxide fuel cells, Chem. Soc. Rev. 37 (2008) 1568–1578.
[46] Q. Wang, J. Hou, Y. Fan, X.-a. Xi, J. Li, Y. Lu, et al., $Pr_2BaNiMnO_{7-\delta}$ double-layered Ruddlesden–Popper perovskite oxides as efficient cathode electrocatalysts for low temperature proton conducting solid oxide fuel cells, J. Mater. Chem. A 8 (2020) 7704–7712.
[47] A.A.A. da Silva, M.C. Steil, F.N. Tabuti, R.C. Rabelo-Neto, F.B. Noronha, L. V. Mattos, et al., The role of the ceria dopant on Ni / doped-ceria anodic layer cermets for direct ethanol solid oxide fuel cell, Int. J. Hydrogen Energy 46 (2021) 4309–4328.
[48] M. Cimenti, J.M. Hill, Direct utilization of ethanol on ceria-based anodes for solid oxide fuel cells, Asia Pac. J. Chem. Eng. 4 (2009) 45–54.
[49] M. Cimenti, J.M. Hill, Direct utilization of methanol and ethanol in solid oxide fuel cells using Cu–Co(Ru)/$Zr_{0.35}Ce_{0.65}O_{2-\delta}$ anodes, J. Power Sources 195 (2010) 3996–4001.
[50] D. La Rosa, M.L. Faro, G. Monforte, V. Antonucci, A.S. Aricò, A. Sin, Recent advances on the development of NiCu alloy catalysts for IT-SOFCs, ECS Trans. 7 (2007) 1685–1693.
[51] C. Sun, U. Stimming, Recent anode advances in solid oxide fuel cells, J. Power Sources 171 (2007) 247–260.
[52] M. Lo Faro, V. Antonucci, P.L. Antonucci, A.S. Aricò, Fuel flexibility: a key challenge for SOFC technology, Fuel 102 (2012) 554–559.
[53] S. Tao, J.T.S. Irvine, A redox-stable efficient anode for solid-oxide fuel cells, Nat Mater. 2 (2003) 320–323.
[54] Y.-H. Huang, R.I. Dass, Z.-L. Xing, J.B. Goodenough, Double perovskites as anode materials for solid-oxide fuel cells, Science 312 (2006) 254–257.
[55] M. Ippommatsu, H. Sasaki, S. Otoshi, Evaluation of the cost performance of the SOFC cell in the market, Int. J. Hydrogen Energy 21 (1996) 129–135.
[56] M. Lo Faro, S. Campagna Zignani, S. Vecino-Mantilla, A.S. Arico', A simple approach to make the commercial solid, oxide fuel cells flexible in the use of fuels – CK-3L05, Ceram. Int. 49 (2023) 24469–24474.
[57] M. Santoro, E. Di Bartolomeo, I. Luisetto, A.S. Aricò, G. Squadrito, S.C. Zignani, et al., Insights on the electrochemical performance of indirect internal reforming of biogas into a solid oxide fuel cell, Electrochim. Acta 409 (2022).
[58] Y.F. Yu Yao, The oxidation of hydrocarbons and CO over metal oxides IV. perovskite-type oxides, J. Catal. 36 (1975) 266–275.
[59] A. Shamsi, K. Zahir, Oxidative-coupling of methane over Perovskite-type oxides and correlation of TMAX for oxygen desorption with C2 selectivity, Preprints Symposia 34 (1989) 544.
[60] T. Shimizu, Partial oxidation of hydrocarbons and oxygenated compounds on perovskite oxides, Catal. Rev. 34 (1992) 355–371.

[61] J.T.S. Irvine, A. Sauvet, Improved oxidation of hydrocarbons with new electrodes in high temperature fuel cells, Fuel Cells 1 (2001) 205–210.
[62] J.S. Kim, J.Y. Lee, J.S. Swinnea, H. Steinfink, W.M. Reiff, P. Lightfoot, et al., Ruddlesden-Popper phases An+1MnO3n+1. Structures and properties, NIST Spec. Publ. (1991) 301–306.
[63] S. Vecino-Mantilla, P. Gauthier-Maradei, M. Huvé, J.M. Serra, P. Roussel, G. H. Gauthier, Nickel exsolution-driven phase transformation from an n=2 to an n=1 Ruddlesden-Popper manganite for methane Steam Reforming reaction in SOFC conditions, ChemCatChem 11 (2019) 4631–4641.
[64] X. Xu, Y. Pan, Y. Zhong, R. Ran, Z. Shao, Ruddlesden–Popper perovskites in electrocatalysis, Mater. Horiz. 7 (2020) 2519–2565.
[65] N.A. Szaro, S.C. Ammal, F. Chen, A. Heyden, Theoretical investigation of the electrochemical oxidation of H_2 and CO fuels on a Ruddlesden–Popper $SrLaFeO_{4-\delta}$ anode, ACS Appl. Mater. Interfaces 15 (2023) 30139–30151.
[66] P. Ding, W. Li, H. Zhao, C. Wu, L. Zhao, B. Dong, et al., Review on Ruddlesden–Popper perovskites as cathode for solid oxide fuel cells, J. Phys.: Mater. 4 (2021) 022002.
[67] S. Vecino-Mantilla, F.M. Lo, Exsolved perovskites for reliable SOFCs fed with dry biogas, Int. J. Hydrogen Energy (2024).
[68] A. Sin, Y. Dubitsky, A. Zaopo, A.S. Aricò, L. Gullo, D. La Rosa, et al., Preparation and sintering of $Ce_{1-x}Gd_xO_{2-x/2}$ nanopowders and their electrochemical and EPR characterization, Solid State Ion. 175 (2004) 361–366.
[69] V.V. Kharton, F.M. Figueiredo, L. Navarro, E.N. Naumovich, A.V. Kovalevsky, A. A. Yaremchenko, et al., Ceria-based materials for solid oxide fuel cells, J. Mater. Sci. 36 (2001) 1105–1117.
[70] H.C. Yao, Y.F.Y. Yao, Ceria in automotive exhaust catalysts I. oxygen storage, J. Catal. 86 (1984) 254–265.
[71] SOFCMAN. Anode-Supported Cells.
[72] S. Vecino-Mantilla, F.M. Lo, A doped cobaltite for enhanced SOFCs fed with dry biogas, Electrochim. Acta 464 (2023) 142927.
[73] M. Lo Faro, D. La Rosa, I. Nicotera, V. Antonucci, A.S. Aricò, Electrochemical behaviour of propane-fed solid oxide fuel cells based on low Ni content anode catalysts, Electrochim. Acta 54 (2009) 5280–5285.
[74] F. d'Acapito, G.O. Lepore, A. Puri, A. Laloni, F. La Manna, E. Dettona, et al., The LISA beamline at ESRF, J. Synchrotron Radiat. 26 (2019) 551–558.
[75] W.T. Elam, J.P. Kirkland, R.A. Neiser, P.D. Wolf, Depth dependence for extended x-ray-absorption fine-structure spectroscopy detected via electron yield in He and in vacuum, Phys. Rev. B 38 (1988) 26–30.
[76] B. Ravel, M. Newville, ATHENA, ARTEMIS, HEPHAESTUS: data analysis for X-ray absorption spectroscopy using IFEFFIT, J. Synchrotron Radiat. 12 (2005) 537–541.
[77] A.L. Ankudinov, J.J. Rehr, Theory of solid-state contributions to the x-ray elastic scattering amplitude, Phys. Rev. B 62 (2000) 2437–2445.
[78] M. Lo Faro, S. Trocino, S.C. Zignani, C. Italiano, R.M. Reis, E.A. Ticianelli, et al., Nickel–Iron/Gadolinium-doped Ceria (CGO) composite electrocatalyst as a protective layer for a Solid-Oxide Fuel Cell anode fed with biofuels, ChemCatChem 8 (2016) 648–655.
[79] J.R. Macdonald, W.B. Johnson, Fundamentals of Impedance Spectroscopy. Impedance Spectroscopy: John Wiley & Sons, Inc. (2005) 1-26.
[80] R. Barfod, M. Mogensen, T. Klemensø, A. Hagen, Y.L. Liu, H.P. Vang, Detailed characterization of anode-supported SOFCs by impedance spectroscopy, J. Electrochem. Soc. 154 (2007) B371–B378.
[81] A. Barbucci, M. Viviani, P. Carpanese, D. Vladikova, Z. Stoynov, Impedance analysis of oxygen reduction in SOFC composite electrodes, Electrochim. Acta 51 (2006) 1641–1650.
[82] Y. Lin, Z. Zhan, J. Liu, S.A. Barnett, Direct operation of solid oxide fuel cells with methane fuel, Solid State Ion. 176 (2005) 1827–1835.
[83] S.P. Yoon, J. Han, S.W. Nam, T.-H. Lim, S.-A. Hong, Improvement of anode performance by surface modification for solid oxide fuel cell running on hydrocarbon fuel, J. Power Sources 136 (2004) 30–36.
[84] K. Nikooyeh, R. Clemmer, V. Alzate-Restrepo, J.M. Hill, Effect of hydrogen on carbon formation on Ni/YSZ composites exposed to methane, Appl. Catal. A: Gen. 347 (2008) 106–111.
[85] R. Mohammadi, M. Ghassemi, Y.M. Barzi, J. Pirkandi, The effect of mass transfer on electrochemical impedance of a solid oxide fuel cell anode, J. Solid State Electrochem. 18 (2014) 2815–2827.
[86] M. Lo Faro, V. Modafferi, P. Frontera, P. Antonucci, A.S. Aricò, Catalytic behavior of Ni-modified perovskite and doped ceria composite catalyst for the conversion of odorized propane to syngas, Fuel Process. Technol. 113 (2013) 28–33.
[87] A. Puri, The LISA XAS database, (2024).
[88] R.K. Li, C. Greaves, Synthesis and characterization of the electron-doped single-layer manganite $La_{1.2}Sr_{0.8}MnO_{4-\delta}$ and Its oxidized phase $La_{1.2}Sr_{0.8}MnO_{4+\delta}$, J. Solid State Chem. 153 (2000) 34–40.